Large magnetoresistance and first-order phase transition in antiferromagnetic single-crystalline $EuAg_4Sb_2$

Sudip Malick [1,2,*] Hanna Świątek [1,2] Joanna Bławat [3] John Singleton [3] and Tomasz Klimczuk [1,2,†]

[1]*Faculty of Applied Physics and Mathematics, Gdansk University of Technology, Narutowicza 11/12, 80-233 Gdansk, Poland*

[2]*Advanced Materials Center, Gdansk University of Technology, Narutowicza 11/12, 80-233 Gdansk, Poland*

[3]*National High Magnetic Field Laboratory, Los Alamos National Laboratory, Los Alamos, New Mexico 87545, USA*

(Received 12 June 2024; revised 16 August 2024; accepted 24 September 2024; published 21 October 2024)

We present the results of a thorough investigation of the physical properties of $EuAg_4Sb_2$ single crystals using magnetization, heat capacity, and electrical resistivity measurements. High-quality single crystals, which crystallize in a trigonal structure with space group $R\bar{3}m$, were grown using a conventional flux method. Temperature-dependent magnetization measurements along different crystallographic orientations confirm two antiferromagnetic phase transitions around $T_{N1} = 10.5$ K and $T_{N2} = 7.5$ K. Isothermal magnetization data exhibit several metamagnetic transitions below these transition temperatures. Antiferromagnetic phase transitions in $EuAg_4Sb_2$ are further confirmed by two sharp peaks in the temperature-dependent heat capacity data at T_{N1} and T_{N2}, which shift to lower temperature in the presence of an external magnetic field. Our systematic heat capacity measurements utilizing a long-pulse and single-slope analysis technique allow us to detect a first-order phase transition in $EuAg_4Sb_2$ at 7.5 K. The temperature-dependent electrical resistivity data also manifest two features associated with magnetic order. The magnetoresistance exhibits a broad hump due to a field-induced metamagnetic transition. Remarkably, the magnetoresistance keeps increasing without showing any tendency to saturate as the applied magnetic field increases, and it reaches ~20 000% at 1.6 K and 60 T. At high magnetic fields, several magnetic quantum oscillations are observed, indicating a complex Fermi surface. A large negative magnetoresistance of about −55% is also observed near T_{N1}. Moreover, the H-T phase diagram constructed using magnetization, heat capacity, and magnetotransport data indicates complex magnetic behavior in $EuAg_4Sb_2$.

DOI: 10.1103/PhysRevB.110.165149

I. INTRODUCTION

Even though there is a lack of single-ion anisotropy in divalent europium ($S = 7/2$ and $L = 0$), which results in negligible crystalline electric field effects, its compounds often manifest intriguing magnetic phase transitions, leading to complex magnetic phase diagrams. Thus, Eu-based intermetallics have always been fascinating candidates for exploring complex magnetism [1–8]. Meanwhile, the discovery of chiral magnetic anomalies, the anomalous Hall effect, and the topological Hall effect in magnetic topological materials has drawn significant attention to Eu-based compounds as they offer an ideal platform for studying the interplay between magnetism and band topology [9–13]. $EuCd_2As_2$, $EuMg_2Bi_2$, $EuMnBi_2$, $EuMnSb_2$, EuTAs (T = Au and Ag), and EuB_6 are a few examples of such magnetic topological materials [6,14–22]. Recently, the trigonal $CaCu_4P_2$-type Eu-based ternary pnictide has received significant attention, as this family of compounds reveals several interesting physical properties. For instance, two successive antiferromagnetic transitions below 15 K and several metamagnetic transitions under applied magnetic field are observed in $EuAg_4As_2$ [23]. Interestingly, the system goes to an incommensurate noncollinear antiferromagnetic (AFM) state below 9 K, exhibiting an anomalous Hall effect. It also shows unusual magnetoresistance (MR) with large positive and negative values. The MR reaches 202% at 2 K and −78% around 10 K at 9 T. Similar magnetotransport behavior is observed in ferromagnetic $EuCu_4As_2$ [24]. On the other hand, the nonmagnetic members of this series, such as SrT_4P_2 (T = Ag and Cu, P = As and Sb), $CaCu_4As_2$, and $SrCu_{4-x}P_2$, also feature several remarkable physical properties. For example, a phase transition associated with a structural distortion is observed in $SrAg_4As_2$, which also shows quantum oscillations associated with small Fermi pockets. Intriguingly, some of the compounds, such as $SrAg_4Sb_2$, $CaCu_4As_2$, and $SrCu_{4-x}P_2$, host nontrivial band topology, which results in the observation of large nonsaturating magnetoresistance, quantum oscillations, and the multilayer quantum Hall effect [25–29].

Here we explore another compound, $EuAg_4Sb_2$, from the same family, which is the magnetic analog of $SrAg_4Sb_2$ and has the potential to show complex magnetic behavior and topological phenomena. An earlier investigation revealed that $EuAg_4Sb_2$ crystallizes in a $CaCu_4P_2$-type centrosymmetric trigonal structure with space group $R\bar{3}m$ (No. 166); it orders antiferromagnetically below 11 K and exhibits a metamagnetic transition at 0.24 T [30]. However, there has not been a detailed investigation of the physical properties of single crystals. This paper thoroughly investigates the physical properties of single crystals of $EuAg_4Sb_2$ along

*Contact author: sudip.malick@pg.edu.pl

†Contact author: tomasz.klimczuk@pg.edu.pl

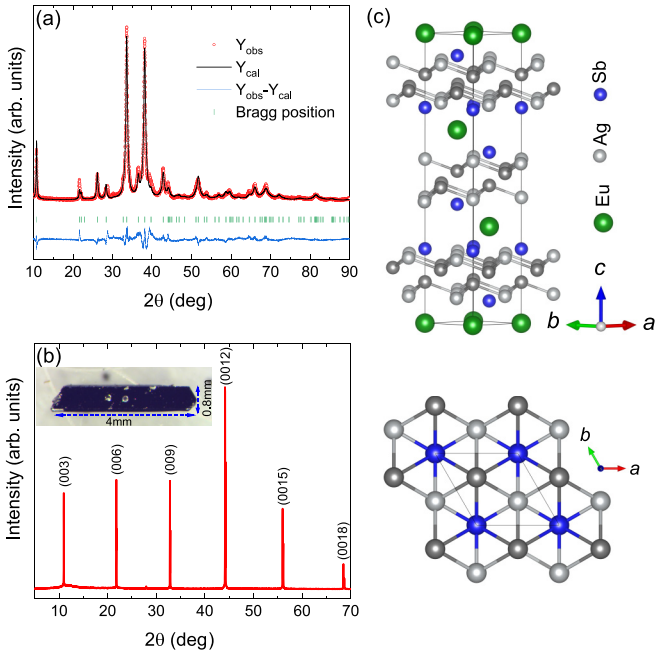

FIG. 1. (a) Powder XRD pattern of the crushed single crystals with the Rietveld refinement analysis. The red dots are the experimentally observed data, and the black line is the calculated XRD pattern from the analysis. The blue line represents the difference between the intensities of experimental and calculated data. Green vertical lines are the Bragg positions. (b) Single-crystal XRD pattern. The inset shows an optical image of a single crystal. (c) A schematic diagram of the crystal structure of $EuAg_4Sb_2$.

different crystallographic orientations using magnetic, thermodynamic, and magnetotransport measurements. Magnetic measurements reveal two antiferromagnetic phase transitions and multiple metamagnetic phase transitions. Temperature-dependent heat capacity and resistivity measurements further corroborate the magnetic phase transitions in $EuAg_4Sb_2$. Careful heat capacity measurements allow us to detect a first-order phase transition at 7.5 K. We have observed unusually large positive and negative magnetoresistance in $EuAg_4Sb_2$. The constructed magnetic phase diagram suggests a complex magnetic structure for $EuAg_4Sb_2$.

II. EXPERIMENTAL DETAILS

The single crystals of $EuAg_4Sb_2$ were grown using a Ag-Sb binary flux as described in Ref. [26] for $SrAg_4Sb_2$. High-purity Eu (99.9%, Onyxmet), Ag (99.999%, Alfa Aesar), and Sb (99.999%, Alfa Aesar) were taken in a 1:7:4 molar ratio. All the elements were mixed thoroughly and put into an alumina crucible. The crucible was sealed in a quartz ampule with partial argon pressure. The ampule was then heated to 1000 °C for 10 h and slowly cooled down to 600 °C at a rate of 1.5 °C/h. The ampule was taken out of the furnace at 600 °C, and the crystals were separated from the flux by centrifuging. An optical image of a single crystal is displayed in the inset in Fig. 1(b). The crystal structure was confirmed by x-ray diffraction (XRD) using a Bruker D2Phaser diffractometer with Cu $K\alpha_1$ radiation. The chemical composition was checked by energy dispersive x-ray spectroscopy (EDS) employing a FEI Quanta FEG 250 electron microscope. All the physical properties of the compound were measured in a Quantum Design EverCool-II physical property measurement system (PPMS). Electrical resistivity measurements were performed using conventional four-probe techniques. Measurements of heat capacity were carried out using the short and long heat pulse method on the PPMS platform. Magnetic measurements were conducted using a vibrating sample magnetometer attached to the PPMS. Note that no demagnetization factor correction was applied to the magnetic data. The high magnetic field data were taken at the pulsed-field facility of the National High Magnetic Field Laboratory (Los Alamos). We performed proximity detector oscillator (PDO) measurements using a 10-turn pancake coil made of 50-gauge copper wire. The coil was connected to the PDO circuit with a resonant frequency of 26 MHz. The technique is sensitive to the skin depth and therefore can be used to probe changes in conductivity, including magnetic quantum oscillations [31,32]. The magnetoresistivity measurements were performed using the standard four-probe technique. An AC current of 1 mA was applied at $f = 100$ kHz.

III. RESULTS AND DISCUSSION

A. Crystal structure

The powder and single-crystal XRD patterns collected at room temperature are presented in Figs. 1(a) and 1(b), respectively. The powder XRD pattern was analyzed using the Rietveld refinement method in the FULLPROF software, which suggests $EuAg_4Sb_2$ crystallizes in a trigonal structure with space group $R\bar{3}m$ (No. 166), which can be derived from the $CaAl_2Si_2$ [33] structure type by placing two additional silver atoms within the slab, creating $[Ag_4Sb_2]^{-2}$ layers. A schematic diagram of the crystal structure is shown in Fig. 1(c). Within each layer, the Ag1 and Ag2 atoms form buckled hexagons, which can be seen in the lower part of Fig. 1(c). The estimated lattice parameters from the refinement are $a = 4.7189(3)$ Å and $c = 24.661(3)$ Å, which agree well with the previous report [30]. The details of the crystallographic parameters are presented in the Supplemental Material (SM) [34]. Figure 1(b) shows the single-crystal XRD pattern of $EuAg_4Sb_2$, which has extremely sharp reflections along $(00c)$ directions, suggesting that the crystallographic c axis is perpendicular to the flat plane of the single crystals. The sharp peaks indicate the high crystalline quality of the grown single crystals. Additionally, EDS data acquired from various points on the single crystals confirm the expected stoichiometry.

B. Magnetic properties

Magnetization M data for various applied fields H in the zero-field-cooled (ZFC) and field-cooled (FC) configurations in the temperature range 2–30 K for the $H \parallel ab$ and $H \parallel c$ crystallographic directions for a $EuAg_4Sb_2$ single crystal are presented in Figs. 2(a) and 2(b), respectively. The temperature-dependent M/H data at 0.1 T along both crystallographic directions show a cusp and a kink around $T_{N1} = 10.6$ K and $T_{N2} = 7.5$ K, respectively, indicating AFM phase transitions. A similar temperature dependence of magnetic

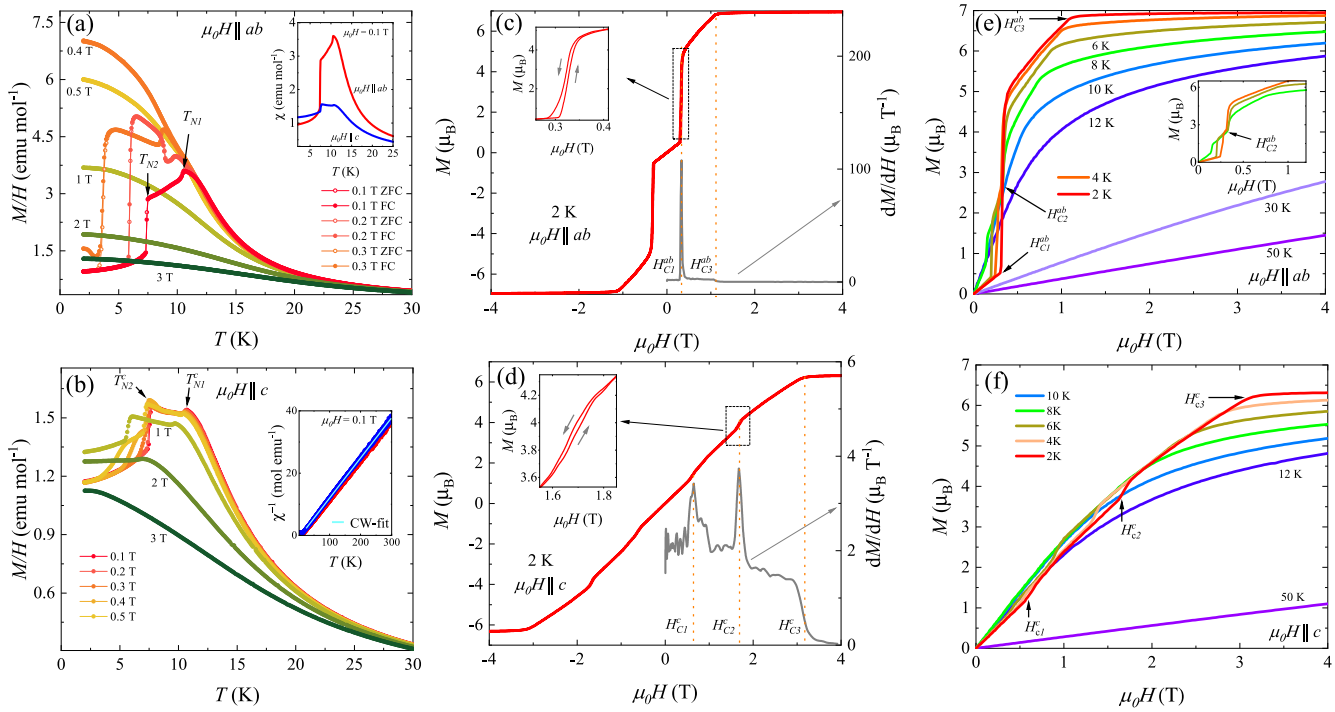

FIG. 2. Magnetic properties of single-crystal $EuAg_4Sb_2$: (a) and (b) M/H data as a function of temperature for various fields applied along the $H \parallel ab$ and $H \parallel c$ crystallographic orientations, respectively. The inset of (a) shows the magnetic susceptibility in the 2–25 K temperature range for $\mu_0H = 0.1$ T along different crystallographic directions. Inverse susceptibility and CW fits up to room temperature are presented for both directions in the inset of (b). Isothermal magnetization for magnetic fields of up to ± 4 T at 2 K applied along (c) $H \parallel ab$ and (d) $H \parallel c$. The insets in both (c) and (d) show an enlarged view of the $M(H)$ data, revealing a hysteresis loop. The right axes of (c) and (d) exhibit the first-order derivative of the $M(H)$ data, indicating the critical fields. Magnetization data at various temperatures up to 4 T for (e) $H \parallel ab$ and (f) $H \parallel c$. The inset of (e) indicates the critical field H^{ab}_{C2}.

susceptibility ($\chi = M/H$) was also observed previously in polycrystalline $EuAg_4Sb_2$ [30]. As the applied field strength increases, T_{N1} and T_{N2} shift to a lower temperature, a typical signature of an AFM [35]. Both anomalies are smeared out for fields $\mu_0H \geqslant 0.4$ T and $\mu_0H \geqslant 3$ T along $H \parallel ab$ and $H \parallel c$, respectively. Interestingly, a slight bifurcation is observed at low temperatures at $\mu_0H = 0.4$ T for $H \parallel ab$ in the ZFC and FC data, probably due to a field-induced metamagnetic (MM) transition. However, in the $H \parallel c$ direction, no irreversible behavior is seen between the ZFC and FC data. The magnetic susceptibility near the ordering increases significantly along $H \parallel ab$ compared to the $H \parallel c$ direction, as illustrated in the inset of Fig. 2(a). On the other hand, at low temperatures (below T_{N2}), χ is larger along $H \parallel c$; it is nearly independent of temperature and does not drop significantly below the magnetic ordering temperature, as expected for a typical AFM. All these features suggest that Eu^{2+} moments likely lie in the ab plane and indicate a noncollinear incommensurate magnetic structure, as observed in the isostructural Eu-based compound $EuAg_4As_2$ [23,36]. Moreover, at temperatures above magnetic order, the $\chi(T)$ data can be described using the Curie-Weiss (CW) law:

$$\chi(T) = \frac{C}{T - \Theta_P}, \tag{1}$$

where C is the Curie constant and Θ_P is the Curie temperature. The inset of Fig. 2(b) shows a fit of the CW law to the $\chi^{-1}(T)$ data measured at 0.1 T in the temperature range 20–300 K. The estimated values of the effective moment and Curie temperature are presented in Table I. The effective moment obtained is close to the theoretical value for the Eu^{2+} ion ($g\sqrt{S(S+1)} = 7.94\mu_B$, $S = 7/2$, and $g = 2$). The fitted Θ_P is positive for both crystallographic directions, as observed in the polycrystalline sample, indicating a predominance of ferromagnetic exchange interactions in the paramagnetic state of $EuAg_4Sb_2$ [30].

Figures 2(c) and 2(d) show the magnetization data acquired at 2 K for fields of up to ± 4 T applied along the $H \parallel ab$ and $H \parallel c$ crystallographic orientations. As the magnetic field increases, the magnetization initially increases linearly, consistent with expectations for an AFM, but around $\mu_0H^{ab}_{C1} = 0.33$ T ($H \parallel ab$) and $\mu_0H^{c}_{C1} = 0.65$ T ($H \parallel c$) there is a sudden jump in magnetization. For a field larger than H_{C1}, M increases linearly until $\mu_0H^{c}_{C2} = 1.67$ T for $H \parallel c$, where it shows another jump in the magnetization. With a further increase of applied field strength, the magnetization saturates

TABLE I. The estimated effective moment and Curie temperature along different crystallographic orientations obtained from the CW fit.

	$H \parallel ab$	$H \parallel c$
μ_{eff} (in units of μ_B)	7.91(1)	7.86(1)
Θ_P (K)	14.2(2)	7.6(1)

near $\mu_0 H_{C3}^{ab} = 1.13\,\mathrm{T}$ and $\mu_0 H_{C3}^{c} = 3.16\,\mathrm{T}$. The saturation values are $6.3\mu_B$ ($H \parallel ab$) and $6.9\mu_B$ ($H \parallel c$), close to the theoretical value $gS\mu_B = 7\mu_B$ for the Eu^{2+} ion. The derivative of M as a function of $\mu_0 H$, depicted on the right axis of Fig. 2(c), reveals the critical fields where those magnetization jumps occur. Such jumps in magnetization are due to field-induced metamagnetic transitions. Interestingly, a hysteresis loop is seen in the metamagnetic transition corresponding to $\mu_0 H_{C2}^{ab}$ and $\mu_0 H_{C1}^{c}$ for increasing and decreasing fields, as illustrated in the insets of Figs. 2(c) and 2(d), respectively. The observed hysteresis around the metamagnetic transitions indicates that these phase transitions are likely first order [37]. We also measured magnetization at various temperatures to get more insight into these transitions, as shown in Figs. 2(e) and 2(f). As the temperature increases, all the critical fields shift to lower values, and the observed anomalies disappear. Surprisingly, along $H \parallel ab$, an additional metamagnetic transition emerges at $\mu_0 H_{C2}^{ab} \sim 0.3\,\mathrm{T}$ for $T \geqslant 4$ K and persists up to 10 K. For $T > 30$ K, which is well above the magnetic ordering temperature, the magnetization increases linearly, as one anticipates for a paramagnetic state at relatively low magnetic fields. Notably, the behavior of $M(H)$ data closely resembles that of the isostructural compound $EuAg_4As_2$, which reveals an incommensurate, noncollinear AFM state at low temperatures, as confirmed by a neutron diffraction study [23,36]. Therefore, a thorough investigation using neutron diffraction measurements is important to understand the complex magnetic structure of $EuAg_4Sb_2$. Nevertheless, similar behavior of the magnetization isotherms is also observed in Eu-based compounds like $Eu_3Ni_4Ga_4$ [38], $EuFe_2As_2$ [39], and EuCuAs [40].

C. Heat capacity

Figure 3(a) shows the zero-field heat capacity C_P data at constant pressure as a function of temperature. At low temperatures, $C_P(T)$ exhibits two sharp anomalies at $T_{N1} = 10.5$ K and $T_{N2} = 7.5$ K as a manifestation of AFM transitions, as observed in the magnetic susceptibility data. The anomaly at T_{N2} is extremely sharp, indicating a first-order phase transition, whereas the AFM transition at T_{N1} is likely a second-order phase transition. A more detailed discussion of these transitions is given later. The behavior of the $C_P(T)$ above the magnetic ordering temperature can be well replicated by considering the Debye (C_D) and Einstein (C_E) models of specific heat, as combined in the following equation [35]:

$$C_P(T) = \gamma T + mC_D + (1-m)C_E. \tag{2}$$

The first term of the above equation is the electronic contribution to the heat capacity. γ is known as the Sommerfeld coefficient. The weight factor m establishes the proportionate contributions between C_D and C_E to the total heat capacity. We use the semiempirical method used in Ref. [35] to treat the heat capacity of the related material $EuMg_2Bi_2$. C_D and C_E are formulated as

$$C_D = 9nR\left(\frac{T}{\Theta_D}\right)^3 \int_0^{\Theta_D/T} \frac{x^4 e^x}{(e^x-1)^2} dx, \tag{3}$$

$$C_E = 3nR\left(\frac{\Theta_E}{T}\right)^2 \frac{e^{\Theta_E/T}}{(e^{\Theta_E/T}-1)^2}. \tag{4}$$

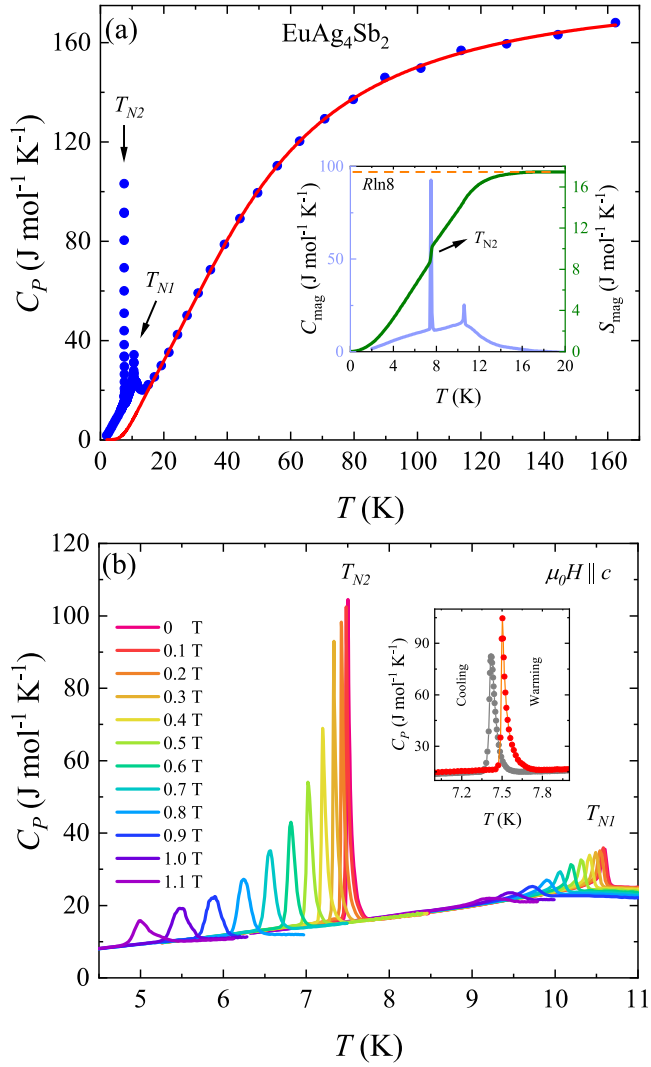

FIG. 3. (a) The temperature dependence of heat capacity in the absence of external magnetic field measured in the temperature range 2–160 K. The red solid line represents the fitting of the data with Eq. (2). The inset shows the magnetic heat capacity and the calculated magnetic entropy. (b) The evolution of the anomalies in the heat capacity under applied magnetic field ranging from 0 to 1.1 T with a step of 0.1 T for $H \parallel c$. The inset depicts the zero-field $C_P(T)$ data obtained from the warming and cooling cycles near T_{N2}.

Here Θ_D and Θ_E are the Debye and Einstein temperatures, respectively. The variable x is defined as $x = \dfrac{\hbar\omega}{k_B T}$, where ω is the phonon frequency. Fitting Eq. (2) to the heat capacity data yields $\gamma = 22.3\,\mathrm{mJ\,mol^{-1}\,K^{-1}}$, $m = 0.79$, $\Theta_D = 208$ K, and $\Theta_E = 50$ K. The obtained fitting parameters are comparable to the isostructural compound $EuCu_4As_2$ [24]. To get a rough estimation of magnetic entropy, we extrapolated the fitting to 2 K and subtracted it from the experimental data to obtain the magnetic component C_{mag} of the heat capacity. The inset of Fig. 3(a) shows the magnetic entropy computed using the expression $S_{\mathrm{mag}} = \int \frac{C_{\mathrm{mag}}}{T} dT$. The magnetic entropy at T_{N1} is about $14.5\,\mathrm{J\,mol^{-1}\,K^{-1}}$, and it increases further as temperature increases and saturates around 16 K to an expected value of $S_{\mathrm{mag}} = R\ln(2S+1) = R\ln 8$ for the Eu^{2+} ion.

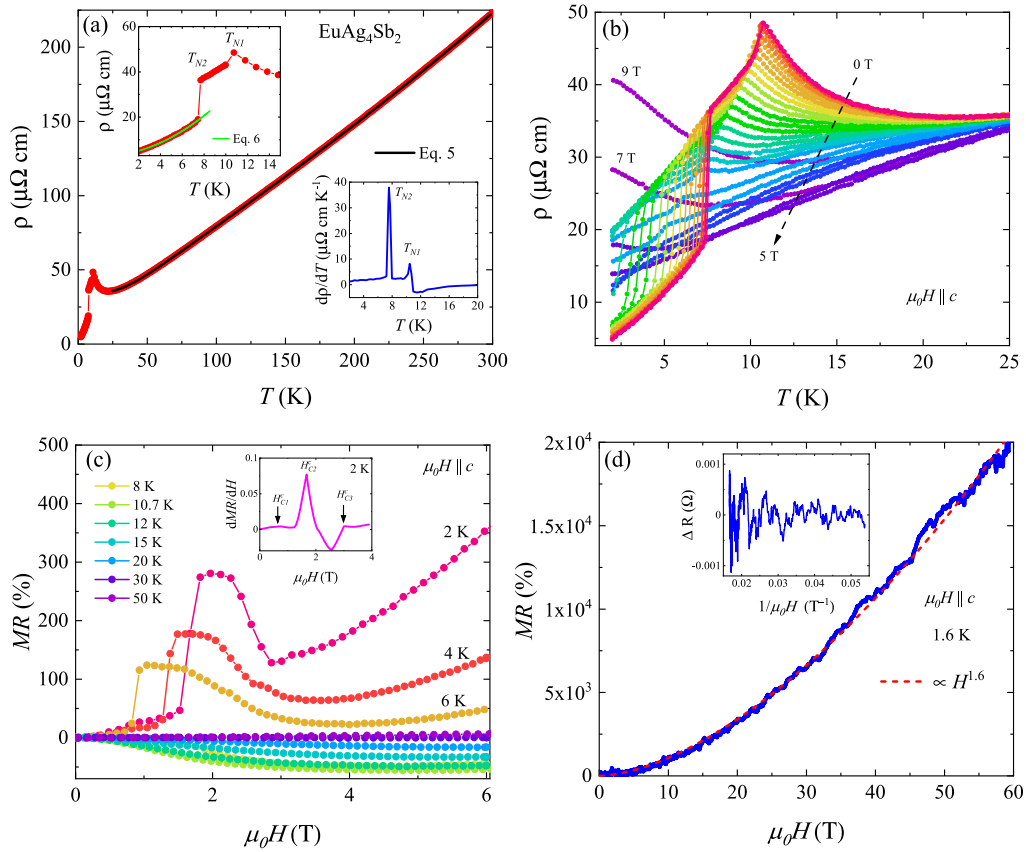

FIG. 4. (a) Zero-field electrical resistivity over the temperature range 2–300 K. The top inset shows an expanded view of $\rho(T)$ at low temperatures, highlighting the features due to the AFM transitions at T_{N1} and T_{N2}. The solid green line represents Eq. (6). The bottom inset describes the first derivative of electrical resistivity as a function of temperature, where peaks represent magnetic phase transitions. (b) Temperature-dependent electrical resistivity under various applied fields, $0 \leqslant \mu_0 H \leqslant 9$ T, where $H \parallel c$. (c) Magnetoresistance as a function of magnetic field applied along $H \parallel c$ at selected temperatures between 2 and 50 K. The inset shows the first derivative of MR as a function of the field, indicating the critical fields. (d) Field-dependent MR data up to 60 T at 1.6 K. The dashed red line demonstrates that MR follows the $H^{1.6}$ field dependence in the high-field region. The inset displays a clear quantum oscillation after a smooth background subtraction.

All the low-temperature heat capacity data presented in Fig. 3 were measured using the long heat pulse technique, and the data were extracted from the single-slope analysis method of the Quantum Design PPMS, which is one of the most effective ways to identify a first-order phase transition [41]. The observed peak at T_{N2} is extremely sharp, having a FWHM of less than 0.1 K. In addition, a thermal hysteresis of around 0.16 K appears in the warming and cooling cycle of the $C_P(T)$ data, as shown in the inset of Fig. 3(b). Remarkably, a discontinuity in temperature-dependent magnetic entropy at T_{N2} can be seen in the inset of Fig. 3(a). All of these observations support the first-order nature of the AFM transition below T_{N2} [42,43]. Figure 3(b) depicts $C_P(T)$ at low temperatures for various applied fields. Both features shifted to lower temperatures, with peaks broadening as the magnetic field intensity increased, which is a typical characteristic of an antiferromagnet.

D. Magnetotransport

The electrical resistivity $\rho(T)$ as a function of temperature measured in zero magnetic field for current along the *ab* plane in the $EuAg_4Sb_2$ single crystal is shown in Fig. 4(a). $\rho(T)$ decreases monotonically with decreasing temperature in a metallic fashion down to 25 K; then it starts to increase and exhibits a peak at 10.7 K and a kink at 7.5 K as the system goes through two antiferromagnetic phase transitions at these temperatures. Two sharp peaks in the first derivative of $\rho(T)$ data, as shown in the bottom inset of Fig. 4(a), further confirm the magnetic phase transitions in $EuAg_4Sb_2$. Remarkably, the $d\rho/dT$ vs T data at low temperatures closely mimic the magnetic specific heat seen in the inset of Fig. 3(a), agreeing with the theoretical model by Fisher and Langer [44]. The residual resistivity ratio [RRR $= \rho(300\,\mathrm{K})/\rho(2\,\mathrm{K})$] ~ 50, is very high, suggesting the very good quality of the as-grown single crystals. A similar RRR value is also found in the nonmagnetic analog compound $SrAg_4Sb_2$ [26]. The behavior of $\rho(T)$ above the magnetic ordering temperature can be well explained by considering electron-phonon (ep) and electron-electron (ee) scattering, as described by [45]

$$\rho(T) = \rho_0 + 4R\left(\frac{T}{\Theta_R}\right)^5 \int_0^{\Theta_R/T} \frac{x^5}{(e^x - 1)(1 - e^{-x})} dx + aT^2, \tag{5}$$

where the first term is the temperature-independent residual resistivity, the second term is the Bloch-Gruneisen scattering model, which accounts for *e*p scattering, and the last term is the contribution from the *ee* scattering. The fit parameters are $\rho_0 = 34\,\mu\Omega\,\text{cm}$, $R = 404\,\mu\Omega\,\text{cm}$, $\Theta_R = 202\,\text{K}$, and $a = 4.7 \times 10^{-4}\,\mu\Omega\,\text{cm K}^{-2}$. The Debye temperature obtained is close to that estimated from the heat capacity data. As per the a and γ values, $EuAg_4Sb_2$ is located near the transition metal line in the Kadowaki-Woods plot presented in the SM [34]. An alternative scattering model considering T^3 dependence is discussed in the SM [34]. Moreover, the temperature dependence of the electrical resistivity below T_{N2}, as shown in the top inset of Fig. 4(a), can be attributed to the scattering of conduction electrons by antiferromagnetic magnons following the formula [46]

$$\rho(T) = \rho_0 + A\Delta^{3/2}T^{1/2}e^{-\Delta/T}\left[1 + \frac{2}{3}\left(\frac{T}{\Delta}\right) + \frac{2}{15}\left(\frac{T}{\Delta}\right)^2\right]. \tag{6}$$

The spin-wave gap Δ and the coefficient A are estimated to be 3.3 K and $0.43\,\mu\Omega\,\text{cm K}^{-2}$, respectively.

In order to determine the effect of the magnetic field on the electrical resistivity, we conducted a systematic field-dependent measurement in the temperature range 2–25 K with the field applied along $H \parallel c$, as displayed in Fig. 4(b). As field strength increases, the ordering temperatures shift to lower values, and both anomalies gradually disappear, in agreement with magnetic susceptibility data. At $\mu_0 H = 3$ T, all resistivity peaks disappear, suggesting metallic behavior. Interestingly, there is a large positive magnetoresistance at low temperatures for $\mu_0 H \geqslant 4$ T; at 2 K and 9 T, the resistivity reaches $40.6\,\mu\Omega\,\text{cm}$. Consequently, we measured MR at several temperatures with the field applied along the c axis, as shown in Fig. 4(c). MR is calculated using the formula $\text{MR} = \frac{\rho(H)-\rho(0)}{\rho(0)} \times 100\%$, where $\rho(0)$ and $\rho(H)$ are the resistivity values in the absence and presence of the external magnetic field. The MR measured at 2 K grows slowly with increasing field, but at about 1.6 T, there is a significant jump in MR, resulting in a broad hump which shifts to lower fields as the temperature increases, in accordance with the $M(H)$ data. The abrupt increase in MR can be attributed to increased magnetic scattering due to metamagnetic transitions. A significant additional contribution to the resistivity on crossing the boundary of the antiferromagnetic phase is likely to come from the rearrangement of the Fermi surface as the magnetic unit cell changes, resulting in an alteration of the density of states available for scattering close to the Fermi energy [47]. The $\text{dMR}/\text{d}H$ vs $\mu_0 H$ data, as presented in the inset of Fig. 4(c), exhibit three peaks, which indicate three critical fields associated with the metamagnetic transitions observed in the magnetization data. MR at low temperatures continues to increase without showing any saturation. For $\mu_0 H > 3$, all the spins are ferromagnetically aligned in the field direction, as indicated by the magnetization; thus, one may anticipate saturation or a decrease in the MR at high applied fields. Nevertheless, as the temperature increases, the MR starts to decrease, and near the ordering temperature, it becomes negative due to the suppression of magnetic scattering. At T_{N1}, it shows a maximum negative MR of about -55%. Once the temperature increases beyond the ordering temperature, the MR starts to increase again. However, at temperatures well above magnetic order, MR is nearly independent of the external magnetic field. Such behavior of MR near the ordering temperature is primarily due to the response of magnetic scattering to the external field, as observed in the similar Eu-based compounds $EuAg_4As_2$ and $EuCu_4As_2$ [23,24]. In order to investigate the high-field behavior of the sample, additional measurements up to 60 T were performed at 1.6 K. The MR continues to increase even at the highest field and reaches a very large value of $\sim$20 000%, as shown in Fig. 4(d). Moreover, MR follows a $H^{1.6}$ field dependence, unlike the semiclassical H^2 dependence [48]. A large MR is also observed in a similar compound, $EuCu_4As_2$, and its origin has been attributed to a nontrivial band structure [24]. Likewise, nonmagnetic $SrAg_4Sb_2$ exhibits unusually high MR due to its nontrivial topological states [26]. Thus, the large nonsaturating MR and its deviation from the quadratic field dependence in $EuAg_4Sb_2$ may result from a nontrivial band structure. The high-field MR data also indicate the presence of quantum oscillations with multiple frequencies, suggesting a complex Fermi surface.

Figure 5(a) shows quantum oscillations after background subtraction using a polynomial function in the contactless electrical resistivity data of $EuAg_4Sb_2$ measured using the proximity detector oscillator technique at high magnetic fields ($12 \leqslant \mu_0 H \leqslant 60$ T) and in the temperature range 0.68–60 K. The PDO measurement detects Shubnikov–de Haas oscillations in the electrical resistivity via the change in resonant frequency f of the oscillator circuit due to changes in the skin depth of the sample. The fast Fourier transform (FFT), shown in Fig. 5(b), reveals several fundamental frequencies and their harmonics. The cyclotron effective mass can be calculated by fitting the FFT amplitude to the temperature-dependent part of the Lifshitz-Kosevich formula [49]:

$$A(T, B_m) \propto \frac{14.69 m^* T/B_m}{\sinh(14.69 m^* T/B_m)}, \tag{7}$$

where B_m is the inverse-field midpoint of the field window used for the FFT, defined as

$$B_m = \left[\frac{1}{2}\left(\frac{1}{B_l} + \frac{1}{B_u}\right)\right]^{-1} \tag{8}$$

Here B_l and B_u are the lower and upper field limits of the window, respectively. The estimated value of the effective mass and its corresponding frequency are presented in Table II. Frequency F_α exhibits unusual temperature dependence, which limits the estimation of effective mass and is subject to further study. Using the Onsager relation $F = (\hbar/2\pi e)A_F$, we calculated the cross-sectional areas of the Fermi surface A_F perpendicular to the applied magnetic field. Further, under the assumption of a circular Fermi-surface cross section, we estimated the Fermi wave vectors k_F and the Fermi velocities v_F presented in Table II using the expressions $k_F = \sqrt{2eF/\hbar}$ and $v_F = \hbar k_F/m^*$, respectively, where $\hbar$ is the reduced Planck's constant and e is the magnitude of electron charge.

TABLE II. The parameters obtained from the quantum oscillation.

	F_α	F_β	F_γ	F_δ	F_σ	F_η
Frequency (T)	22	160	193	1120	1273	1460
m^* (in units of m_e)		0.16 ± 0.01	0.19 ± 0.01	0.67 ± 0.05	0.68 ± 0.05	0.64 ± 0.04
A_F (nm^{-2})	0.21	1.53	1.84	10.70	12.16	13.94
k_F (nm^{-1})	0.26	0.70	0.77	1.84	1.97	2.11
v_F ($10^6 ms^{-1}$)		0.51	0.47	0.32	0.34	0.38

E. *H-T* phase diagram

To get an overall picture of the magnetic behavior of $EuAg_4Sb_2$ at low temperatures, we constructed an *H-T* phase diagram based on the magnetic, heat capacity, and magneto-transport measurements for the field orientations $H \parallel ab$ and $H \parallel c$, as presented in Figs. 6(a) and 6(b), respectively. The overall *H-T* phase diagram can be divided into six domains. As the temperature decreases from room temperature, the system enters the first antiferromagnetic (AFM1) state from the paramagnetic (PM) state around 10.5 K. With a further decrease in temperature, the system exhibits a first-order AFM phase transition, as confirmed by the heat capacity data. The region below this transition is labeled AFM2. Both ordering temperatures shift to lower temperatures with increasing magnetic field, forming a distinct phase diagram boundary in accordance with the molecular field theory expression

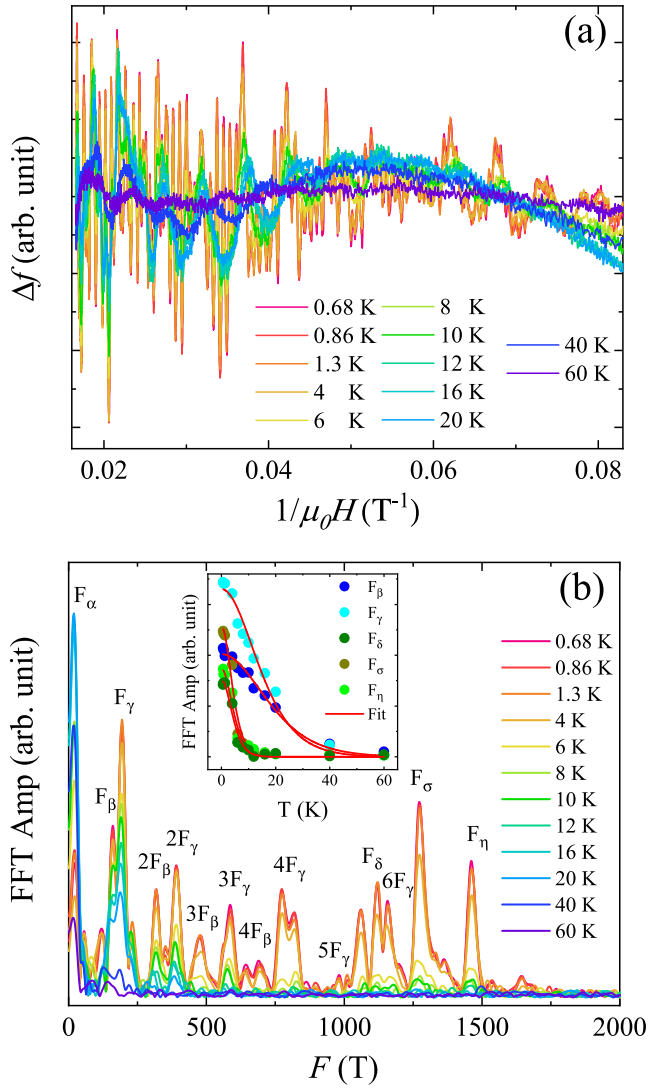

FIG. 5. (a) PDO data as a function of $1/\mu_0 H$ after smooth background subtraction measured in a 12 T window along $H \parallel c$. (b) The frequency-dependent FFT signals measured at various temperatures. The inset shows the fitting of the FFT amplitude to Eq. (7).

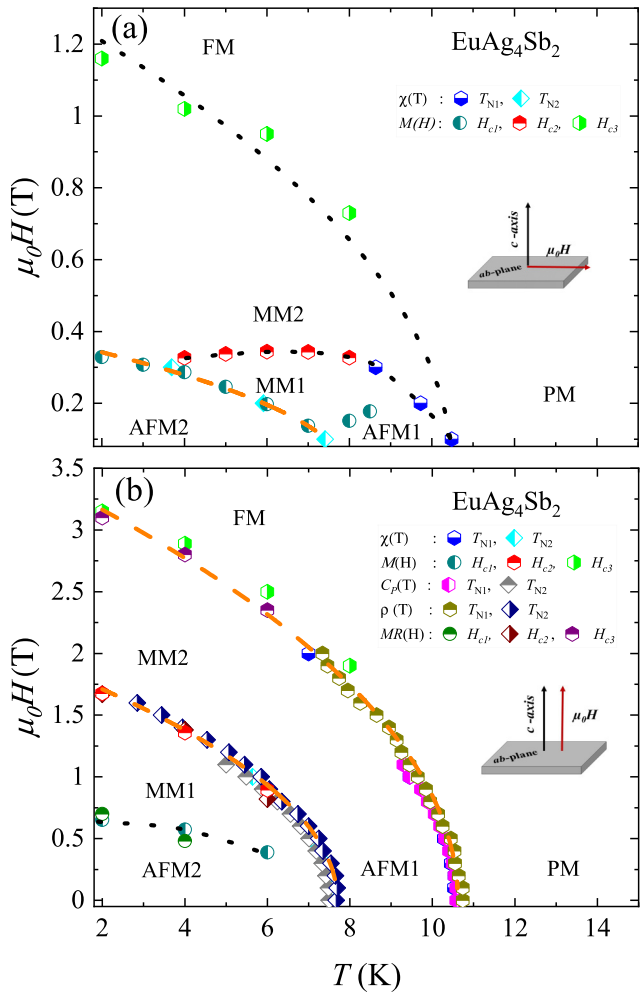

FIG. 6. Magnetic phase diagram of a $EuAg_4Sb_2$ single crystal for the (a) $H \parallel ab$ and (b) $H \parallel c$ orientations, constructed using magnetization, heat capacity, and magnetotransport data. Black dotted lines are the hand drawn as visual guides. Orange dashed lines originate from the molecular field theory expression given in the text.

$H = H_0[1 - T_N(H)/T_N(H = 0)]^{1/2}$, where H_0 is the critical field that destroys the antiferromagnetic transitions at 0 K [50]. The estimated value of $\mu_0 H_0$ for $H \parallel ab$ is 0.39 T (T_{N2}), whereas for $H \parallel c$, $\mu_0 H_0 = 3.5$ T (T_{N1}) and 1.98 T (T_{N2}). When a magnetic field of H_{C1} is applied to the system within the AFM2 regime, the system undergoes a metamagnetic transition (MM1). For $H \parallel ab$, the phase boundaries MM1 and AFM2 overlap with each other. However, for $H \parallel c$, MM1 and AFM2 create two separate regions. Another metamagnetic transition (MM2) occurs when the magnetic field hits H_{C2}. These MM transitions are most likely the results of spin-flop transitions [37]. At low temperatures (below 6 K), the AFM2 and MM2 phase boundaries overlap in the case of $H \parallel c$. As the applied magnetic field increases further, the system undergoes another transition at H_{C3}, at which point all spins align along the field direction; it behaves like a ferromagnet (FM). Interestingly, for $H \parallel c$, the phase boundary for H_{C3} at higher fields almost overlaps with the first AFM transition. However, we could not clearly distinguish between PM and FM states based on the available data.

IV. CONCLUSION

We studied the magnetic, thermodynamic, and electrical transport properties of high-quality single-crystal $EuAg_4Sb_2$ grown using Ag-Sb binary flux. The XRD data confirmed that $EuAg_4Sb_2$ crystallizes in a trigonal structure. Our comprehensive analysis of temperature-dependent magnetization, electrical resistivity, and heat capacity data revealed that $EuAg_4Sb_2$ orders antiferromagnetically at 10.5 and 7.5 K. The transition at 7.5 K is identified as a first-order phase transition using systematic heat capacity measurements performed with the long heat pulse technique. Several metamagnetic transitions were observed in the isothermal magnetization data. Further investigation using neutron diffraction measurements is required to fully understand the complex magnetic structure of $EuAg_4Sb_2$. Interestingly, MR displays nonsaturation behavior at low temperatures, which reaches a very large value of ~20 000% at 1.6 K and 60 T. Moreover, as the temperature rises, the MR decreases and becomes negative. Near the first AFM phase transition, a large negative value of about 55% was observed. In addition, the field-dependent magnetoresistance showed a hump as a characteristic of metamagnetic transitions. At high magnetic fields, several magnetic quantum oscillations were observed, indicating a complex Fermi surface. Our findings on $EuAg_4Sb_2$ indicate that it is an antiferromagnetic system with a complex magnetic structure and a potential topological material.

ACKNOWLEDGMENTS

The work at Gdansk University of Technology was supported by the National Science Center (Poland), Grant No. 2022/45/B/ST5/03916. A portion of this work was performed at the National High Magnetic Field Laboratory, which is supported by National Science Foundation Cooperative Agreement No. DMR-2128556, the U.S. Department of Energy (DoE), and the state of Florida. J.B. and J.S. acknowledge support from the DoE Basic Energy Science Field Work Proposal "Science of 100 T," which permitted development of some of the high-field techniques used in this paper.

[1] K. Sengupta, P. L. Paulose, E. V. Sampathkumaran, T. Doert, and J. P. F. Jemetio, Magnetic behavior of $EuCu_2As_2$: A delicate balance between antiferromagnetic and ferromagnetic order, Phys. Rev. B **72**, 184424 (2005).

[2] H. S. Jeevan, Z. Hossain, D. Kasinathan, H. Rosner, C. Geibel, and P. Gegenwart, Electrical resistivity and specific heat of single-crystalline $EuFe_2As_2$: A magnetic homologue of $SrFe_2As_2$, Phys. Rev. B **78**, 052502 (2008).

[3] W. T. Jin, Y. Xiao, S. Nandi, S. Price, Y. Su, K. Schmalzl, W. Schmidt, T. Chatterji, A. Thamizhavel, and T. Brückel, Coexistence of Eu antiferromagnetism and pressure-induced superconductivity in single-crystal $EuFe_2As_2$, Phys. Rev. B **100**, 014503 (2019).

[4] U. B. Paramanik, P. L. Paulose, S. Ramakrishnan, A. K. Nigam, C. Geibel, and Z. Hossain, Magnetic and superconducting properties of Ir-doped $EuFe_2As_2$, Supercond. Sci. Technol. **27**, 075012 (2014).

[5] R. Pöttgen and D. Johrendt, Equiatomic intermetallic europium compounds: Syntheses, crystal chemistry, chemical bonding, and physical properties, Chem. Mater. **12**, 875 (2000).

[6] S. Malick, J. Singh, A. Laha, V. Kanchana, Z. Hossain, and D. Kaczorowski, Electronic structure and physical properties of EuAuAs single crystal, Phys. Rev. B **105**, 045103 (2022).

[7] S. Seiro and C. Geibel, Complex and strongly anisotropic magnetism in the pure spin system $EuRh_2Si_2$, J. Phys.: Condens. Matter **26**, 046002 (2014).

[8] O. Bednarchuk and D. Kaczorowski, Strongly anisotropic and complex magnetic behavior in $EuRhGe_3$, J. Alloys Compd. **646**, 291 (2015).

[9] B. A. Bernevig, C. Felser, and H. Beidenkopf, Progress and prospects in magnetic topological materials, Nature (London) **603**, 41 (2022).

[10] Y. Tokura, K. Yasuda, and A. Tsukazaki, Magnetic topological insulators, Nat. Rev. Phys. **1**, 126 (2019).

[11] B. Yan and C. Felser, Topological materials: Weyl semimetals, Annu. Rev. Condens. Matter Phys. **8**, 337 (2017).

[12] G. Chang, B. Singh, S.-Y. Xu, G. Bian, S.-M. Huang, C.-H. Hsu, I. Belopolski, N. Alidoust, D. S. Sanchez, H. Zheng, H. Lu, X. Zhang, Y. Bian, T.-R. Chang, H.-T. Jeng, A. Bansil, H. Hsu, S. Jia, T. Neupert, H. Lin, Magnetic and noncentrosymmetric Weyl fermion semimetals in the *R*AlGe family of compounds (R = rare earth), Phys. Rev. B **97**, 041104(R) (2018).

[13] P. K. Rout, P. V. P. Madduri, S. K. Manna, and A. K. Nayak, Field-induced topological Hall effect in the noncoplanar triangular antiferromagnetic geometry of Mn_3Sn, Phys. Rev. B **99**, 094430 (2019).

[14] J. Ma, H. Wang, S. Nie, C. Yi, Y. Xu, H. Li, J. Jandke, W. Wulfhekel, Y. Huang, D. West, P. Richard, A. Chikina, V. N. Strocov, J. Mesot, H. Weng, S. Zhang, Y. Shi, T. Qian, M. Shi, and H. Ding, Emergence of nontrivial low-energy dirac fermions in antiferromagnetic $EuCd_2As_2$, Adv. Mater. **32**, 1907565 (2020).

[15] S. Roychowdhury, M. Yao, K. Samanta, S. Bae, D. Chen, S. Ju, A. Raghavan, N. Kumar, P. Constantinou, S. N. Guin, N. C. Plumb, M. Romanelli, H. Borrmann, M. G. Vergniory, V. N. Strocov, V. Madhavan, C. Shekhar, and C. Felser, Anomalous Hall conductivity and Nernst effect of the ideal Weyl semimetallic ferromagnet $EuCd_2As_2$, Adv. Sci. **10**, 2207121 (2023).

[16] M. Marshall, I. Pletikosić, M. Yahyavi, H.-J. Tien, T.-R. Chang, H. Cao, and W. Xie, Magnetic and electronic structures of antiferromagnetic topological material candidate $EuMg_2Bi_2$, J. Appl. Phys. **129**, 035106 (2021).

[17] M. Kondo, M. Ochi, R. Kurihara, A. Miyake, Y. Yamasaki, M. Tokunaga, H. Nakao, K. Kuroki, T. Kida, M. Hagiwara, H. Murakawa, N. Hanasaki, and H. Sakai, Field-tunable Weyl points and large anomalous Hall effect in the degenerate magnetic semiconductor $EuMg_2Bi_2$, Phys. Rev. B **107**, L121112 (2023).

[18] H. Masuda, H. Sakai, M. Tokunaga, M. Ochi, H. Takahashi, K. Akiba, A. Miyake, K. Kuroki, Y. Tokura, and S. Ishiwata, Impact of antiferromagnetic order on Landau-level splitting of quasi-two-dimensional Dirac fermions in $EuMnBi_2$, Phys. Rev. B **98**, 161108(R) (2018).

[19] K. Zhao, X. Chen, Z. Wang, J. Liu, J. Wu, C. Xi, X. Lv, L. Li, Z. Zhong, and P. Gegenwart, Magnetic tuning of band topology evidenced by exotic quantum oscillations in the Dirac semimetal $EuMnSb_2$, Phys. Rev. B **107**, L081112 (2023).

[20] A. Laha, R. Singha, S. Mardanya, B. Singh, A. Agarwal, P. Mandal, and Z. Hossain, Topological Hall effect in the antiferromagnetic Dirac semimetal EuAgAs, Phys. Rev. B **103**, L241112 (2021).

[21] S. Nie, Y. Sun, F. B. Prinz, Z. Wang, H. Weng, Z. Fang, and X. Dai, Magnetic semimetals and quantized anomalous Hall effect in EuB_6, Phys. Rev. Lett. **124**, 076403 (2020).

[22] S.-Y. Gao, S. Xu, H. Li, C.-J. Yi, S.-M. Nie, Z.-C. Rao, H. Wang, Q.-X. Hu, X.-Z. Chen, W.-H. Fan, J.-R. Huang, Y.-B. Huang, N. Pryds, M. Shi, Z.-J. Wang, Y.-G. Shi, T.-L. Xia, T. Qian, and H. Ding, Time-reversal symmetry breaking driven topological phase transition in EuB_6, Phys. Rev. X **11**, 021016 (2021).

[23] Q. Zhu, L. Li, Z. Yang, Z. Lou, J. Du, J. Yang, B. Chen, H. Wang, and M. Fang, Metamagnetic transitions and anomalous magnetoresistance in $EuAg_4As_2$ crystals, Sci. China: Phys. Mech. Astron. **64**, 227011 (2021).

[24] L. Li, Z. Yang, Q. Su, J. Yang, B. Chen, J. Du, C. Wu, H. Wang, and M. Fang, Large positive and negative magnetoresistance in the magnetic $EuCu_4As_2$ crystal, J. Alloys Compd. **916**, 165460 (2022).

[25] B. Shen, E. Emmanouilidou, X. Deng, A. McCollam, J. Xing, G. Kotliar, A. I. Coldea, and N. Ni, Significant change in the electronic behavior associated with structural distortions in monocrystalline $SrAg_4As_2$, Phys. Rev. B **98**, 235130 (2018).

[26] Y. Nie, W. Tu, Y. Yang, Z. Chen, Y. Wang, S. Pan, M. Mei, X. Zhu, W. Lu, W. Ning, and M. Tian, Quantum oscillations and nontrivial topological properties of layered metal $SrAg_4Sb_2$, Appl. Phys. Lett. **123**, 163101 (2023).

[27] Y. Nie, Z. Chen, W. Wei, H. Li, Y. Zhang, M. Mei, Y. Wang, W. Song, D. Song, Z. Wang, X. Zhu, W. Ning, and M. Tian, Linear magnetoresistance and structural distortion in layered $SrCu_{4-x}P_2$ single crystals, Chin. Phys. B **33**, 016108 (2024).

[28] Y. Nie, Z. Chen, M. Mei, Y.-Y. Wang, J.-T. Wu, J.-L. Jiang, W.-H. Song, W. Ning, Z.-S. Wang, X.-D. Zhu, and M.-L. Tian, Subtle lattice distortion-driven phase transitions in layered ACu_4As_2 (A = Eu, Sr), Chin. Phys. B **32**, 106102 (2023).

[29] S. Sasmal, V. Saini, S. Ramakrishnan, G. Dwari, B. B. Maity, J.-K. Bao, R. Mondal, V. Tripathi, S. van Smaalen, B. Singh, and A. Thamizhavel, Observation of multilayer quantum Hall effect in the charge density wave material $CaCu_4As_2$, Phys. Rev. Res. **4**, L012011 (2022).

[30] B. Gerke, C. Schwickert, S. S. Stoyko, M. Khatun, A. Mar, and R. Pottgen, Magnetic hyperfine field splitting in $EuAg_4As_2$ and $EuAg_4Sb_2$, Solid State Sci. **20**, 65 (2013).

[31] S. Ghannadzadeh, M. Coak, I. Franke, P. A. Goddard, J. Singleton, and J. L. Manson, Measurement of magnetic susceptibility in pulsed magnetic fields using a proximity detector oscillator, Rev. Sci. Instrum. **82**, 113902 (2011).

[32] K. Götze, M. J. Pearce, P. A. Goddard, M. Jaime, M. B. Maple, K. Sasmal, T. Yanagisawa, A. McCollam, T. Khouri, P.-C. Ho, and J. Singleton, Unusual phase boundary of the magnetic-field-tuned valence transition in $CeOs_4Sb_{12}$, Phys. Rev. B **101**, 075102 (2020).

[33] E. Gladishevskij, P. Kripjakevic, and O. Bodak, The crystal structures of the compound $CaAl_2Si_2$ and its analogues, Ukr. Fiz. Zh. (Ukr. Ed.) **12**, 447 (1967).

[34] See Supplemental Material at http://link.aps.org/supplemental/10.1103/PhysRevB.110.165149 for detailed crystallographic parameters, a comparison of different scattering models in the resistivity, and the Kadowaki-Woods plot.

[35] S. Pakhira, M. A. Tanatar, and D. C. Johnston, Magnetic, thermal, and electronic-transport properties of $EuMg_2Bi_2$ single crystals, Phys. Rev. B **101**, 214407 (2020).

[36] B. Shen, C. Hu, H. Cao, X. Gui, E. Emmanouilidou, W. Xie, and N. Ni, Structural distortion and incommensurate noncollinear magnetism in $EuAg_4As_2$, Phys. Rev. Mater. **4**, 064419 (2020).

[37] B. Cheng, B. F. Hu, R. H. Yuan, T. Dong, A. F. Fang, Z. G. Chen, G. Xu, Y. G. Shi, P. Zheng, J. L. Luo, and N. L. Wang, Field-induced spin-flop transitions in single-crystalline $CaCo_2As_2$, Phys. Rev. B **85**, 144426 (2012).

[38] Anupam, C. Geibel, and Z. Hossain, Magnetic behavior of $Eu_3Ni_4Ga_4$: Antiferromagnetic order and large magnetoresistance, J. Phys.: Condens. Matter **24**, 326002 (2012).

[39] S. Jiang, Y. Luo, Z. Ren, Z. Zhu, C. Wang, X. Xu, Q. Tao, G. Cao, and Z. Xu, Metamagnetic transition in $EuFe_2As_2$ single crystals, New J. Phys. **11**, 025007 (2009).

[40] J. Tong, J. Parry, Q. Tao, G.-H. Cao, Z.-A. Xu, and H. Zeng, Magnetic properties of EuCuAs single crystal, J. Alloys Compd. **602**, 26 (2014).

[41] A. Scheie, LongHCPulse: Long-pulse heat capacity on a quantum design PPMS, J. Low Temp. Phys. **193**, 60 (2018).

[42] K. R. Kumar, H. S. Nair, R. Christian, A. Thamizhavel, and A. M. Strydom, Magnetic, specific heat and electrical transport properties of Frank–Kasper cage compounds RTM_2Al_{20}, J. Phys.: Condens. Matter **28**, 436002 (2016).

[43] F. Guillou, A. K. Pathak, D. Paudyal, Y. Mudryk, F. Wilhelm, A. Rogalev, and V. Pecharsky, Non-hysteretic first-order phase transition with large latent heat and giant low-field magnetocaloric effect, Nat. Commun. **9**, 2925 (2018).

[44] M. E. Fisher and J. S. Langer, Resistive anomalies at magnetic critical points, Phys. Rev. Lett. **20**, 665 (1968).

[45] G. v. Minnigerode, Göran Grimvall, E. P. Wohlfahrt (Eds.): *The Electron-Phonon Interaction in Metals*, Vol. 16, aus: *Selected Topics in Solid State Physics*. North Holland Publishing Company, Amsterdam, New York, Oxford 1981. 304 Seiten, Dfl 125,—, Ber. Bunsengesellschaft Phys. Chem. **87**, 453 (1983).

[46] M. A. Continentino, S. N. de Medeiros, M. T. D. Orlando, M. B. Fontes, and E. M. Baggio-Saitovitch, Anisotropic quantum critical behavior in $CeCoGe_{3-x}Si_x$, Phys. Rev. B **64**, 012404 (2001).

[47] R. G. Goodrich, N. Harrison, and Z. Fisk, Fermi surface changes across the Néel phase boundary of NdB_6, Phys. Rev. Lett. **97**, 146404 (2006).

[48] R. Niu and W. K. Zhu, Materials and possible mechanisms of extremely large magnetoresistance: A review, J. Phys.: Condens. Matter **34**, 113001 (2022).

[49] D. Shoenberg, *Magnetic Oscillations in Metals* (Cambridge University Press, Cambridge, 2009).

[50] N. S. Sangeetha, E. Cuervo-Reyes, A. Pandey, and D. C. Johnston, $EuCo_2P_2$: A model molecular-field helical Heisenberg antiferromagnet, Phys. Rev. B **94**, 014422 (2016).